Stability and periodicity of high-order Lorenz–Stenflo equations

2016 Phys. Scr. 91 065202

(http://iopscience.iop.org/1402-4896/91/6/065202)

IOP Publishing | Royal Swedish Academy of Sciences Physica Scripta

Phys. Scr. **91** (2016) 065202 (6pp) doi:10.1088/0031-8949/91/6/065202

Stability and periodicity of high-order Lorenz–Stenflo equations

Junho Park, Beom-Soon Han, Hyunho Lee, Ye-Lim Jeon and Jong-Jin Baik

School of Earth and Environmental Sciences, Seoul National University, Seoul 08826, Korea

E-mail: junho.park@snu.ac.kr

Received 16 April 2016
Accepted for publication 3 May 2016
Published 24 May 2016

Abstract

In this paper, we derive high-order Lorenz–Stenflo equations with 6 variables and investigate periodic behaviors as well as stability of the equations. The stability of the high-order Lorenz–Stenflo equations is investigated by the linear stability analysis for various parameters. A periodicity diagram is also computed and it shows that the high-order Lorenz–Stenflo equations exhibit very different behaviors from the original Lorenz–Stenflo equations for both periodic and chaotic solutions. For example, period 3 regime for large parameters and scattered periodic regime are newly observed, and chaotic regimes exist for smaller values of r but for larger values of s than the original equations. In contrast, similarities such as the enclosure of the chaotic regime by the periodic regime or complex periodic regimes inside the chaotic regime are also observed for both the original and high-order Lorenz–Stenflo equations.

Keywords: Lorenz–Stenflo equations, stability, periodicity, nonlinear dynamics

(Some figures may appear in colour only in the online journal)

1. Introduction

Stenflo [1] derived a simple set of nonlinear ordinary differential equations, now known as the Lorenz–Stenflo equations, from the equations for atmospheric acoustic-gravity waves. The Lorenz–Stenflo equations consist of the following equations:

$$\dot{X} = \sigma(Y - X) + sV, \tag{1}$$

$$\dot{Y} = rX - XZ - Y, \tag{2}$$

$$\dot{Z} = XY - bZ, \tag{3}$$

$$\dot{V} = -X - \sigma V, \tag{4}$$

where X, Y, Z and V are the dynamical variables, dot denotes the derivative with respect to the time t, σ is the Prandtl number, r is the generalized Rayleigh parameter, b is the geometric parameter, and s is the rotation parameter. This set of equations is regarded as the extended Lorenz equations since it reduces to the Lorenz equations [2] when the rotation parameter s is zero, and it also can be derived from the rotating thermal convection equations. Various dynamic features such as stability [3], bifurcation [4, 5], or periodic [6] and chaotic behaviors [7] of the Lorenz–Stenflo equations have been thoroughly studied for decades after Stenflo [1].

Recently, Shen derived the high-order Lorenz equations with five variables [8] and six variables [9] by including additional terms with higher vertical wavenumbers. In this way, nonlinear feedback of the high-order terms to the original Lorenz equations can be investigated. This nonlinear feedback is very important since it can change significantly the stability and bifurcation properties of nonlinear equations [10]. From analyses of the linear stability and the Lyapunov exponents, Shen [8] found that stability of the five-variable Lorenz equations with five variables is increased for the parameter r compared to that of the original Lorenz equations. On the other hand, the six-variable Lorenz equations with six variables are slightly stabilized [9] compared to the five-variable Lorenz equations. This implies that different small scale processes in additional terms act different roles for the stability of the system [9].

In this paper, we derive high-order Lorenz–Stenflo equations by adding terms with higher vertical wavenumbers similar to Shen [8] for the five-variable Lorenz equations. Stability of the high-order Lorenz–Stenflo equations is investigated by the linear stability analysis for various parameters (section 2). In section 3, we numerically investigate

the high-order Lorenz–Stenflo equations by computing the periodicity diagram [6] in the parameter space (r, s) for $\sigma = 10$ and $b = 8/3$. Conclusions are presented in section 4.

2. High-order Lorenz–Stenflo equations

2.1. Derivation of high-order Lorenz–Stenflo equations

We introduce two-dimensional rotating thermal convection equations in $(x-z)$-directions. The governing equations in non-dimensional form [2, 11] are

$$\frac{\partial \nabla^2\psi}{\partial \tau} = \frac{\partial \psi}{\partial z}\frac{\partial \nabla^2\psi}{\partial x} - \frac{\partial \psi}{\partial x}\frac{\partial \nabla^2\psi}{\partial z} - 2\Omega\frac{\partial v}{\partial z} + \mathrm{Ra}\sigma\frac{\partial T}{\partial x} + \sigma\nabla^4\psi, \tag{5}$$

$$\frac{\partial v}{\partial \tau} = \frac{\partial \psi}{\partial z}\frac{\partial v}{\partial x} - \frac{\partial \psi}{\partial x}\frac{\partial v}{\partial z} + 2\Omega\frac{\partial \psi}{\partial z} + \sigma\nabla^2 v, \tag{6}$$

$$\frac{\partial T}{\partial \tau} = \frac{\partial \psi}{\partial z}\frac{\partial T}{\partial x} - \frac{\partial \psi}{\partial x}\frac{\partial T}{\partial z} + \frac{\partial \psi}{\partial x} + \nabla^2 T, \tag{7}$$

where ψ is the stream function, v is the velocity in y-direction, T is the temperature deviated from the mean state, τ is the time, Ω is the angular velocity, $\nabla^2 = \partial^2/\partial x^2 + \partial^2/\partial z^2$, Ra is the Rayleigh number, and σ is the Prandtl number. We consider truncated Galerkin expansions for ψ, v and T as

$$\psi = \psi_A X(t)\sin(k_x x)\sin(k_z z), \tag{8}$$

$$v = v_A V(t)\sin(k_x x)\cos(k_z z), \tag{9}$$

$$T = y_A Y(t)\cos(k_x x)\sin(k_z z) - z_A Z(t)\sin(2k_z z) + y_{1A} Y_1(t)\cos(k_x x)\sin(3k_z z) - z_{1A} Z_1(t)\sin(4k_z z), \tag{10}$$

where k_x and k_z are the wavenumbers in x- and z-directions, respectively, $k^2 = k_x^2 + k_z^2$, $t = k^2\tau$, $\psi_A = \sqrt{2}k^2/(k_x k_z)$, $v_A = -(2\Omega k_z/k^2)\psi_A$, $y_A = y_{1A} = \sqrt{2}k^6/(\mathrm{Ra}k_x^2 k_z)$ and $z_A = z_{1A} = k^6/(k_x^2 k_z \mathrm{Ra})$. In these truncations, the high-order terms with non-zero y_{1A} and z_{1A} are considered only for T following Shen [8]. Note that if $y_{1A} = z_{1A} = 0$, this leads to the original Lorenz–Stenflo equations (1)–(4). Applying (8)–(10) to (5)–(7), we obtain the following high-order Lorenz–Stenflo equations:

$$\dot{X} = \sigma(Y - X) + sV, \tag{11}$$

$$\dot{Y} = rX - XZ - Y, \tag{12}$$

$$\dot{Z} = XY - XY_1 - bZ, \tag{13}$$

$$\dot{V} = -X - \sigma V, \tag{14}$$

$$\dot{Y}_1 = XZ - 2XZ_1 - dY_1, \tag{15}$$

$$\dot{Z}_1 = 2XY_1 - 4bZ_1, \tag{16}$$

where $s = 4\Omega^2 k_z^2/k^6$, $r = \mathrm{Ra}k_x^2/k^6$, $b = 4k_z^2/k^2$ and $d = (k_x^2 + 9k_z^2)/k^2$. Note that the constant d has a relation $d = 1 + 2b$.

Although the above high-order Lorenz–Stenflo equations are derived from the rotating thermal convection equations, they can be also derived similarly from the atmospheric gravity wave equations as done by Stenflo [1]. In the following subsection, the stability of the high-order Lorenz–Stenflo equations is investigated by the linear stability analysis.

2.2. Linear stability analysis

To perform the linear stability analysis, we first need to find fixed points X_0, Y_0, Z_0, V_0, Y_{10} and Z_{10} which can be obtained by applying $\dot{X} = \dot{Y} = \dot{Z} = \dot{V} = \dot{Y}_1 = \dot{Z}_1 = 0$ to (11)–(16). The fixed points are the origin $O = (X, Y, Z, V, Y_1, Z_1) = (0, 0, 0, 0, 0, 0)$ and $P_i = (X_{0i}, Y_{0i}, Z_{0i}, V_{0i}, Y_{10i}, Z_{10i})$, $(i = 1, \ldots, 4)$ which satisfy the following relations:

$$X_0^4 + B_1 X_0^2 + B_2 = 0,$$
$$Y_0 = \left(1 + \frac{s}{\sigma^2}\right)X_0, \quad Z_0 = r - 1 - \frac{s}{\sigma^2},$$
$$V_0 = -\frac{X_0}{\sigma}, \quad Y_{10} = \frac{X_0 Z_0}{d + X_0^2/b},$$
$$Z_{10} = \frac{X_0^2 Z_0}{2b(d + X_0^2/b)}, \tag{17}$$

where $B_1 = b\{d - 2Z_0/(1 + s/\sigma^2)\}$ and $B_2 = -b^2 d Z_0/(1 + s/\sigma^2)$. For convenience, we denote four fixed points $X_{01} = -X_{02} = \sqrt{(-B_1 + \sqrt{B_1^2 - 4B_2})/2}$ and $X_{03} = -X_{04} = \sqrt{(-B_1 - \sqrt{B_1^2 - 4B_2})/2}$. Around the fixed points, we apply perturbations $x' = X - X_0$, $y' = Y - Y_0$, $z' = Z - Z_0$, $v' = V - V_0$, $y'_1 = Y_1 - Y_{10}$ and $z'_1 = Z_1 - Z_{10}$. Then, we obtain linearized equations of perturbations $\vec{v} = (x', y', z', v', y'_1, z'_1)$ as $\mathrm{d}\vec{v}/\mathrm{d}t = \mathbf{A}\vec{v}$ where

$$\mathbf{A} = \begin{bmatrix} -\sigma & \sigma & 0 & s & 0 & 0 \\ r - Z_0 & -1 & -X_0 & 0 & 0 & 0 \\ Y_0 - Y_{10} & X_0 & -b & 0 & -X_0 & 0 \\ -1 & 0 & 0 & -\sigma & 0 & 0 \\ Z_0 - 2Z_{10} & 0 & X_0 & 0 & -d & -2X_0 \\ 2Y_{10} & 0 & 0 & 0 & 2X_0 & -4b \end{bmatrix}. \tag{18}$$

For each fixed point, eigenvalues λ can be obtained by solving the eigenvalue problem $\mathbf{A}\vec{v} = \lambda\vec{v}$, and stability of the high-order Lorenz–Stenflo equations can be determined by the real part of λ (i.e. stable if $\mathrm{Re}(\lambda) < 0$ and unstable if $\mathrm{Re}(\lambda) > 0$). For the fixed point O, the eigenvalue equation of the matrix $\mathbf{A}$ becomes

$$(\lambda + d)(\lambda + 4b)(\lambda + b)(\lambda^3 + A_1\lambda^2 + A_2\lambda + A_3) = 0, \tag{19}$$

where $A_1 = 1 + 2\sigma$, $A_2 = s + \sigma^2 + 2\sigma - r\sigma$ and $A_3 = s - (r - 1)\sigma^2$. Note that four eigenvalues in the last two parentheses are the same as those of the fixed point O for the original Lorenz–Stenflo equations [5] and $\lambda = -d$ and $\lambda = -4b$ are new eigenvalues which appear due to inclusion of the high-order variables Y_1 and Z_1. Since b and d are positive, this implies that stability around the fixed point O for the high-order Lorenz–Stenflo equations is determined by the eigenvalues in the last parentheses thus is the same as that for the original Lorenz–Stenflo equations.

For the fixed points P_i, it is very cumbersome to obtain analytic expressions of eigenvalues so the eigenvalue problem

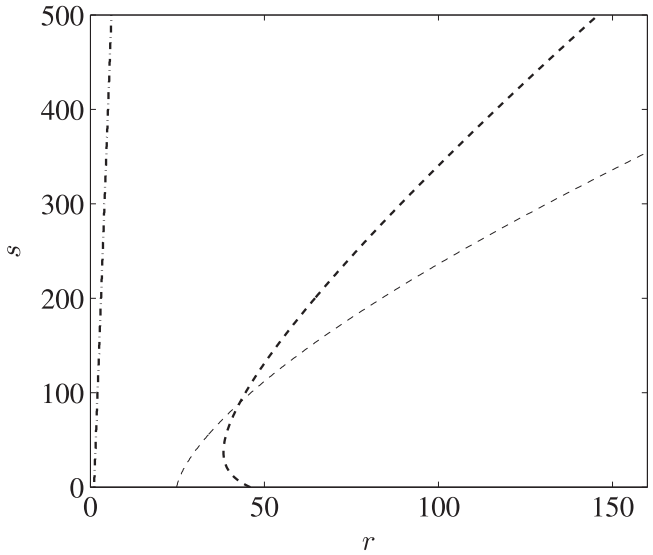

Figure 1. Neutral stability curves of the fixed points O (thick dash–dot line) and $P_{1,2}$ (thick dashed line) in the parameter space (r, s) for $\sigma = 10$ and $b = 8/3$. Thin dashed line represents the neutral stability curve on which the Hopf bifurcation occurs for the original Lorenz–Stenflo equations.

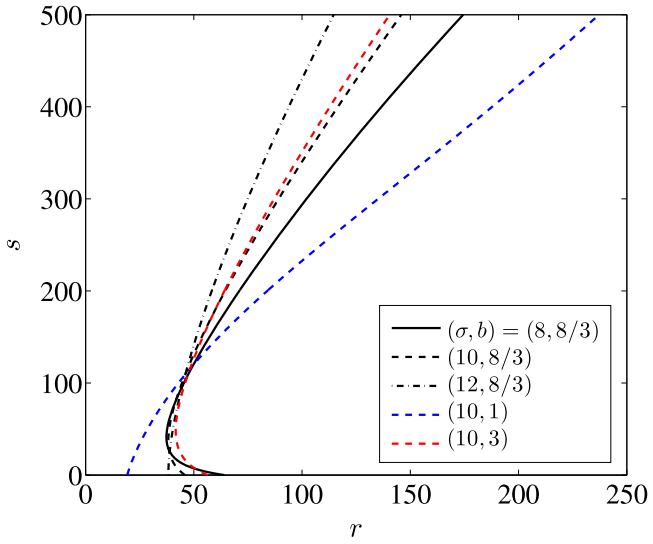

Figure 2. Neutral stability curves of the fixed points $P_{1,2}$ in the parameter space (r, s) for (σ, b): (8, 8/3) (black solid line), (10, 8/3) (black dashed line), (12, 8/3) (black dash–dot line), (10, 1) (blue dashed line) and (10, 3) (red dashed line).

of the matrix $\mathbf{A}$ is numerically solved. Figure 1 shows neutral stability curves, where the real part of λ becomes zero, of the fixed points O and $P_{1,2}$ in the parameter space (r, s) for $\sigma = 10$ and $b = 8/3$. For these parameters, it is found that the fixed points P_3 and P_4 lie in the complex plane so only the stability of the fixed points $P_{1,2}$ is investigated. It is found that the neutral stability curves of P_1 and P_2 are identical. Also, it is found that the neutral stability curve for the fixed points $P_{1,2}$ is very different from that of the Hopf bifurcation, where all the fixed points become unstable, for the original Lorenz–Stenflo equations (1)–(4). For $s = 0$, the fixed points $P_{1,2}$ become unstable when $r > 45.94$, a larger value than the value for the original Lorenz equations $r > 24.74$ [8]. But interestingly, the critical value r on the neutral stability curve decreases as s increases, and it reaches the minimum $r \approx 38.23$ at $s \approx 37$. Then, the critical value r on the stability curve increases with s when $s > 37$. Moreover, it is clearly shown that the high-order Lorenz–Stenflo equations become more unstable for the parameter r than the original Lorenz–Stenflo equations when $s > 89.3$. This is remarkable because the previous study on the high-order Lorenz equations by Shen [8] reveals that the nonlinear feedback is negative so the stability is increased for the parameter r while for the high-order Lorenz–Stenflo equations, inclusion of the rotation parameter s gives the positive nonlinear feedback to the equations as a decrease of the stability.

Figure 2 shows neutral stability curves of the fixed points $P_{1,2}$ in the parameter space (r, s) for different values of the parameters σ and b. It is clearly shown that when $\sigma < 12$ for $b = 8/3$ or when $b > 1$ for $\sigma = 10$, there is a range of s where the critical value r decreases as s increases. However, for all values of the parameters, the critical value r on the stability curve increases with s when s is sufficiently large. This implies that the parameter s for the high-order Lorenz–Stenflo equations acts a role of stabilization when s is sufficiently large, similar to that for the original Lorenz–Stenflo equations. In the next section, numerical investigations on the high-order Lorenz–Stenflo equations (11)–(16) are made.

3. Numerical results

We perform numerical integrations of (11)–(16) using the 4th order Runge–Kutta method with a time resolution $\Delta t = 10^{-4}$. Figure 3 shows time series plots of the variable X for different values of the parameters r and s for $\sigma = 10$ and $b = 8/3$. The initial condition $(X, Y, Z, V, Y_1, Z_1) = (1, 0, 0, 0, 0, 0)$ is used. For $r = 28$ and $s = 0$ (figure 3(a)), the high-order Lorenz–Stenflo equations are stable, and the variable X converges to the fixed point $X_{02} \approx -11.66$ as time goes to infinity. The convergence of X is also observed for other stable cases in figures 3(b) and (c) such that X converges to the fixed points $X_{02} \approx -14.14$ and $X_{01} \approx 9.16$ for (b) and (c), respectively. When the high-order Lorenz–Stenflo equations are unstable (figures 3(d)–(f)), the variable X does not converge to a fixed point but it shows either chaotic behaviors (figures 3(d) and (e)) or periodic behaviors (figure 3(f)) around the fixed points.

For unstable solutions, we obtain the periodicity diagram [6, 12, 13] to investigate periodic and chaotic behaviors in wide ranges of the parameters r and s. We mainly focus on the parameters r and s, and other parameters are fixed as $\sigma = 10$ and $b = 8/3$. The initial condition with $X_0 = 10^{-2}$, $Y_0 = V_0 = Y_{10} = Z_{10} = 0$ and $Z_0 = r$ is used for numerical integrations, and the data are truncated from $t = 0$ to $t = 100$ in order to ignore transient behaviors by the initial condition [4, 6, 14]. Many different initial conditions were also tested, and all the results confirmed that solutions lie on periodic trajectories or chaotic attractors. After $t = 100$, additional numerical integrations are performed from $t = 100$ to

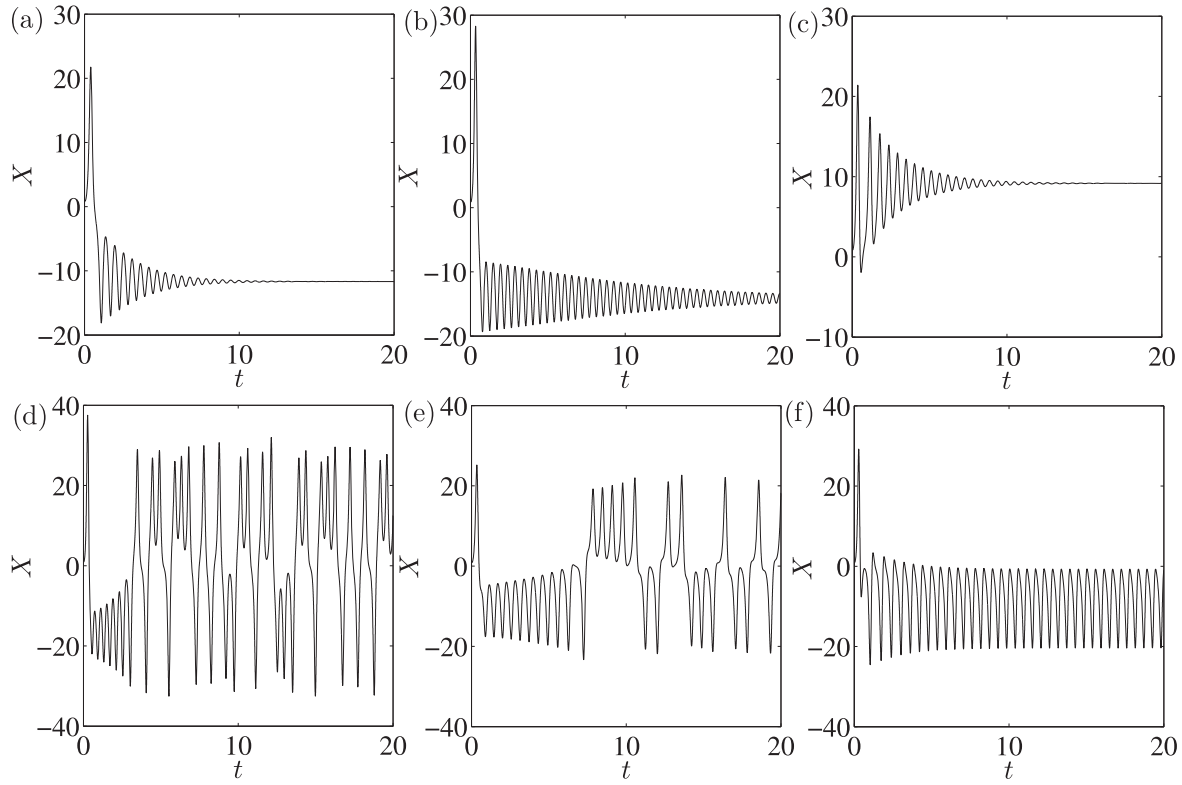

Figure 3. Time series plots of the variable X for $\sigma = 10$ and $b = 8/3$, and for (r, s): (a) (28, 0), (b) (40, 0), (c) (40, 120), (d) (60, 0), (e) (40, 50) and (f) (60, 150).

$t = 120$. This time range is sufficient to capture periodic or chaotic behaviors of solutions in the parameter space of our interest. We define the periodicity as the number of local maximums of the variable Z ($Z_{\max}$) [6, 14]. The local maximums $Z_{\max}$ are picked in the time range $100 \leqslant t \leqslant 120$, and they are regarded as different maximums if they differ with a relative tolerance greater than 0.1% [6, 14].

In figure 4, trajectories on the Y–Z plane for $\sigma = 10$ and $b = 8/3$, and for different values of r and s are displayed. Figure 4(a) shows an example of chaotic solutions. The period cannot be defined for the chaotic solutions since it increases as more time integrations are performed. An example of period 1 solutions is shown in figure 4(b) where there is one local maximum $Z_{\max} = 78.15$. The trajectory in figure 4(c) has period 2 since it has two local maximums $Z_{\max} = 256.01$ and $Z_{\max} = 235.35$. Similarly, figure 4(d) shows an example of solutions with period 4.

Figure 5 shows the periodicity diagram in the r–s parameter space for $\sigma = 10$ and $b = 8/3$. The periodicity diagram is computed with resolutions $\Delta r = \Delta s = 1$. These resolutions are not sufficient to capture very narrow regimes like narrow periodic windows [15], but they are sufficient to see the overall structures of periodic and chaotic regimes in wide ranges of the parameters r and s. The black regime represents the regime of stable solutions and is separated from the unstable regime by a blue dashed line which is the neutral stability curve of $P_{1,2}$ in figure 1. In the unstable regime, solutions with periods from 1 to 16 are distinguished by different colors, and chaotic solutions or solutions with periods higher than 16 are colored by white. As seen in figure 5, regimes with periods from 9 to 16 colored by yellow cover very small areas. This implies that regimes with periods higher than 16 cover even smaller areas and the white regime can be regarded almost as the chaotic regime [6].

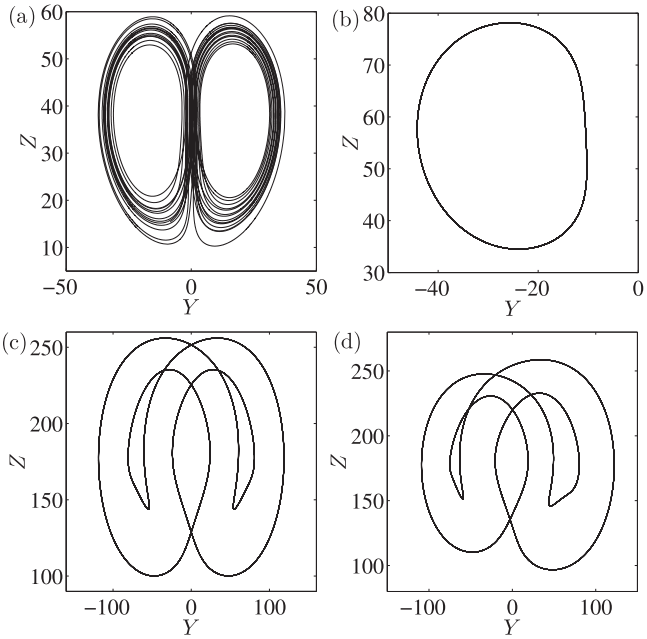

Figure 4. Trajectories on the Y–Z plane for $\sigma = 10$ and $b = 8/3$, and for (a) chaotic solution ($r = 40$, $s = 50$), (b) period 1 solution ($r = 60$, $s = 150$), (c) period 2 solution ($r = 180$, $s = 0$) and (d) period 4 solution ($r = 180$, $s = 10$).

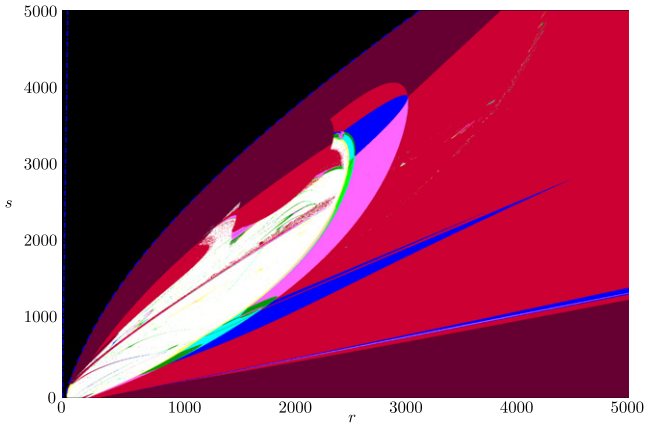

Figure 5. Periodicity diagram in the r–s parameter space ($0 \leqslant r \leqslant 5000$ and $0 \leqslant s \leqslant 5000$) for $\sigma = 10$ and $b = 8/3$. Colors indicate the periodicity of solutions: fixed solutions (black), period 1 (dark red), period 2 (red), period 3 (blue), period 4 (pink), period 5 (green), period 6 (cyan), period 7 (light green), period 8 (light pink), periods 9–16 (yellow). White regions represent solutions with period higher than 16 or chaotic solutions. Blue dash–dot and dashed lines represent curves on which the fixed points O and $P_{1,2}$ become unstable, respectively.

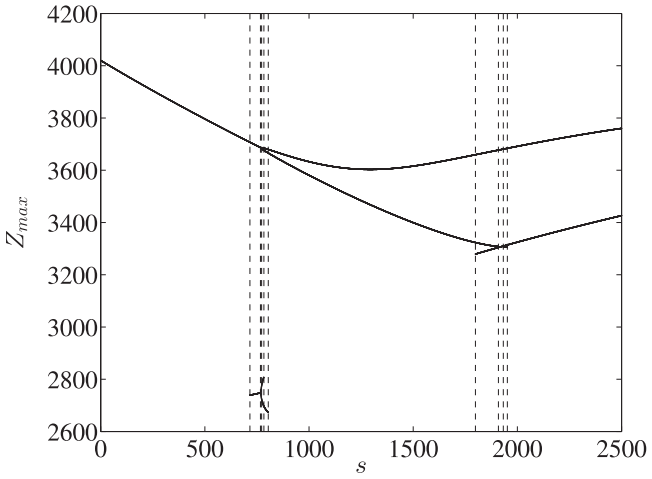

Figure 6. Bifurcation diagram of $Z_{\max}$ as a function of s for $r = 3000$, $\sigma = 10$ and $b = 8/3$. Dashed lines represent locations where the periodicity changes. The interval $\Delta s = 0.25$ is used in this diagram.

Compared to the periodicity diagram of the original Lorenz–Stenflo equations [6], the periodicity diagram of the high-order Lorenz–Stenflo equations shows quite different structures. Firstly, a period 3 regime which extends for large values of r is observed for the high-order Lorenz–Stenflo equations. Secondly, periodic regimes are less observed inside the chaotic regime for the high-order Lorenz–Stenflo equations. Moreover, there are new interesting features such as scattered periodic regime ($1250 \lesssim r \lesssim 1500$, $2000 \lesssim s \lesssim 2500$), discontinuous changes of periodic regimes ($2350 \lesssim r \lesssim 2450$, $3200 \lesssim s \lesssim 3600$), etc. These are not observable for the original Lorenz–Stenflo equations. For the high-order Lorenz–Stenflo equations, the chaotic solutions exist for $r < r_{\max} = 2515$ and $s < s_{\max} = 3336$, and all the solutions outside these ranges are either periodic or fixed. For the original Lorenz–Stenflo equations, $r_{\max} = 2975$ and $s_{\max} = 2340$ [6]. This implies that the stability of the high-order Lorenz–Stenflo equations is increased for the parameter r while it is decreased for the parameter s.

Similar features between the original and high-order Lorenz–Stenflo equations are also observed. First of all, inside the chaotic regime which is enclosed by periodic regimes for large parameters r and s, periodic regimes such as narrow periodic windows, shrimp-shape islands or long bands are well observed similar to the original Lorenz–Stenflo equations [6, 7]. These periodic regimes are frequently observed in other chaotic systems such as the Ehrhard–Müller system [14], the modulated CO_2 laser [16], the Hénon map [17], or the Chua's circuit [18]. Periodicity changes from $2 \to 4 \to 3 \to 2 \to 1$ as s increases in the range $2600 \lesssim r \lesssim 3000$ are also observed for both the original and high-order Lorenz–Stenflo equations.

To understand why the period 3 regime is present for large r, we show in figure 6 the bifurcation diagram of $Z_{\max}$ as a function of s for $r = 3000$, $\sigma = 10$ and $b = 8/3$. Dashed lines represent locations where period of the solutions changes. Interestingly, new bifurcation appears in the range $716 < s < 805$, and this leads to the period 3. This new bifurcation occurs as the trajectories on the Y–Z plane changes, and new maximums around $Z \approx 2740$ appear as s increases. Figure 7 clearly shows how the period of solutions changes and how the symmetry of the trajectory on $Y = 0$ breaks down as s increases. The period changes from 2 to 3 as the new local maximum around $Z_{\max} \approx 2760$ appears (figures (b) and (c)), and it changes from 3 to 4 as the symmetry of the trajectory on $Y = 0$ breaks down (figures (c) and (d)). Then, the period becomes 2 as the local maximum around $Z_{\max} \approx 2690$ disappears (figures (e) and (f)).

4. Conclusions

This paper investigated the high-order Lorenz–Stenflo equations derived from the rotating thermal convection equations by considering two additional Fourier modes with two higher vertical wavenumbers. From the linear stability analysis, it was found that the stability of the high-order Lorenz–Stenflo equations is very different from that of the original Lorenz–Stenflo equations. For the parameters $\sigma = 10$ and $b = 8/3$, the high-order Lorenz–Stenflo equations are more stable than the original Lorenz–Stenflo equations when $s < 89.3$ while they are more unstable when $s > 89.3$. Linear stability of the high-order Lorenz–Stenflo equations is also investigated for different values of the parameters σ and b. In the unstable regime, periodic and chaotic behaviors of the solutions are investigated by the periodicity diagram in wide ranges of the parameters r and s. Similarities with the original Lorenz–Stenflo equations are that there are both chaotic and periodic regimes and the chaotic regime is enclosed by the periodic regimes. Periodic regimes such as narrow periodic windows, shrimp-shape islands or long bands are also observed inside the chaotic regime for the high-order Lorenz–

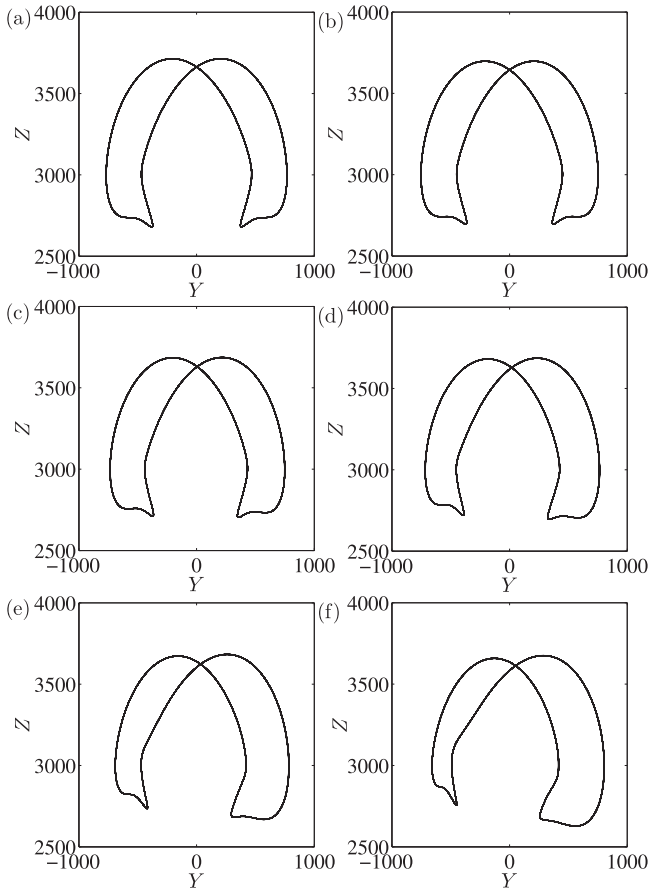

Figure 7. Trajectories on the $Y-Z$ plane for $\sigma = 10$, $b = 8/3$ and $r = 3000$, and for (a) period 1 solution ($s = 700$), (b) period 2 solution ($s = 740$), (c) period 3 solution ($s = 770$), (d) period 4 solution ($s = 775$), (e) period 3 solution ($s = 790$) and (f) period 2 solution ($s = 820$).

Stenflo equations. Differences from the original Lorenz–Stenflo equations are that new interesting regimes such as scattered periodic regime, discontinuous period changes or period 3 regime for large r appear in the high-order Lorenz–Stenflo equations. Moreover, the high-order Lorenz–Stenflo equations can be chaotic for smaller values of r ($r < 2515$) but for larger values of s ($s < 3336$) than the original Lorenz–Stenflo equations. This implies that the inclusion of high-order nonlinear terms can lead to different stability of the equations. This paper also investigated in detail the new period 3 regime which appears due to the transition of trajectories as s increases.

While this study focuses mainly on the periodic behaviors, chaotic behaviors of the high-order Lorenz–Stenflo equations should be investigated as done by Rech [7] for the original Lorenz–Stenflo equations. Theoretical studies such as hyper-chaotic properties [19] or boundedness [20] for the high-order Lorenz–Stenflo equations should also be performed. Moreover, the Lorenz–Stenflo equations with even higher order terms should be investigated since more generalized equations with high order terms can improve the stability or predictability [8, 10] which will be of great interest for people who research on atmospheric gravity waves or thermal convection.

Acknowledgments

The authors were supported by the Korea Meteorological Administration Research and Development Program under grant KMIPA 2015-5190.

References

[1] Stenflo L 1996 *Phys. Scr.* **53** 83–4
[2] Lorenz E N 1963 *J. Atmos. Sci.* **20** 130–41
[3] Yu M Y and Yang B 1996 *Phys. Scr.* **54** 140–2
[4] Yu M Y, Zhou C T and Lai C H 1996 *Phys. Scr.* **54** 321–4
[5] Zhou C, Lai C H and Yu M Y 1997 *J. Math. Phys.* **38** 5225–39
[6] Park J, Lee H, Jeon Y L and Baik J J 2015 *Phys. Scr.* **90** 065201
[7] Rech P C 2015 *Phys. Scr.* **90** 115201
[8] Shen B W 2014 *J. Atmos. Sci.* **71** 1701–23
[9] Shen B W 2015 *Nonlinear Process. Geophys.* **22** 749–64
[10] Curry J H 1978 *Commun. Math. Phys.* **60** 193–204
[11] Saltzman B 1962 *J. Atmos. Sci.* **19** 329–41
[12] Dullin H R, Schmidt S, Richter P H and Grossmann S K 2007 *Int. J. Bifurcation Chaos* **17** 3013–33
[13] Xavier J C and Rech P C 2010 *Int. J. Bifurcation Chaos* **20** 145–52
[14] Park J, Lee H and Baik J J 2016 *Int. J. Bifurcation Chaos* **26** 6
[15] Zhou C, Lai C H and Yu M Y 1997 *Phys. Scr.* **55** 394–402
[16] Gallas J A C 1993 *Phys. Rev. Lett.* **70** 2714–7
[17] Bonatto C, Garreau J C and Gallas J A C 2005 *Phys. Rev. Lett.* **95** 143905
[18] Albuquerque H A, Rubinger R M and Rech P C 2008 *Phys. Lett.* A **372** 4793–8
[19] Wang Z, Zhou L, Chen Z and Wang J 2016 *Nonlinear Dyn.* **83** 2055–66
[20] Zhang F, Wang X, Mu C and Zhang G 2015 *Nonlinear Dyn.* **79** 539–47